Table

Table 1: Important parameters of LHD and HL-2A.

	LHD	HL-2A
Major radius (m)	3.75	1.65
Minor radius (m)	~0.7	0.4
Toroidal field (T)	2.64	1.42
Connection length (m)	10^0-10^4	~50
Input power (MW)	4 - 8	0.1 - 0.4
n_{LCFS} (10^{19} m^{-3})	1 - 6	0.2 - 1.4
Te @ LCFS (eV)	150 - 300	~40
$\nu_{SOL}^{*electron}$ (*1)	3 - 45	0.7 - 15
ν_{SOL}^{*ion} (*2)	1 - 41	0.2 - 6
Θ (*3)	10^{-4} - 10^{-3}	10^{-2} - 10^{-1}

(*1) $\nu_{SOL}^{*electron} = 10^{-16}\, n_{up}\, L_{//} / T_{eup}{}^2$

(*2) $\nu_{SOL}^{*ion} = 10^{-16}\, n_{up}\, L_{//} / T_{iup}{}^2$

LHD : $L_{//}$=L_K (Kolmogorov length) = 10 - 100 m. HL-2A : $L_{//}$=20 m.

(*3) LHD : $\Theta \equiv \vec{b} \cdot \vec{r} \approx B_r / B_\phi$. HL-2A : $\Theta \equiv \vec{b} \cdot \vec{\theta} \approx B_\theta / B_\phi$.

Figure captions

Fig.1 (LHD) (a) Magnetic field structure in confinement region of LHD and configuration of helical coils. Major and averaged minor radii are 3.75 and 0.70 m, respectively. (b) Poloidal cross section of LHD with divertor plates and divertor legs. Color represents the connection length (L_C). Divertor legs come out from confinement region in-between helical coils. (c) L_C distribution in poloidal and minor radial (r_{eff}) coordinate system. r_{eff} is defined by cylindrical approximation of volume enclosed by each radial surface of computational mesh. Dashed lines in (c) indicate boundaries of edge surface layers and stochastic region. In the present analysis, the term of stochastic layer is used to represent the entire edge region including both the edge surface layers and the stochastic region.

Fig.2 (HL-2A) (a) Schematic of HL-2A tokamak in poloidal cross section with vacuum vessel and divertor chamber/baffle. Three multi-pole coils create divertor configuration. Major and minor radii are 1.65 and 0.40 m, respectively. (b) L_C distribution in poloidal cross section. The numerals of 0 to 50 in (b) denote parallel distance, s, in meter along flux tubes with $L_C = 50 \pm 0.5\,m$, mapped to poloidal cross section.

Fig.3 (HL-2A) Parallel profiles of various parameters along the field line of $L_C = 50 \pm 0.5\,m$ for densities of n_{LCFS}=0.3 x10^{19} m^{-3} (a-c) and 0.6 x10^{19} m^{-3} (d-f), respectively. Coordinate s is defined in Fig.2. (b). (a) and (d) show parallel energy flux of electron conduction, $q^e_{//D}$ (solid line), electron convection, $q^e_{//V}$ (dashed line), ion conduction, $q^i_{//D}$ (dotted line) and ion convection, $q^i_{//V}$ (chain line). (b) and (e) show parallel impurity velocity, $V^{imp}_{Z//}$ and contribution of each term on the right hand side of eq.(3), electron thermal force, $V_{//}{}^{the}$ (solid lines), ion thermal force, $V_{//}{}^{thi}$ (dashed lines), friction force, $V_{//}{}^{fric}$ (dashed-dotted lines) and // electric force, $V_{//}{}^{E}$ (dotted lines). For the definition, see the text. Note that the scale of vertical axes of (b) and (e) are different each other by one order of magnitude. (c) and (f) show carbon density summed over all charge states (solid lines) and carbon ionization source (dotted lines). The carbon density (n_{imp}) is normalized at the divertor plate (n_{imp_down}). Negative values of energy flux and velocity indicate direction towards outer divertor plates. X-point is located around s=5 m.

Fig.4 (HL-2A) (a) Two dimensional distribution of carbon density summed over all charge states and (b) force balance of $|V_{//}^{fric}|-|V_{//}^{thi}|$ in HL-2A, for n_{LCFS}=0.25 x10^{19} m^{-3} (upper) and 0.60 x10^{19} m^{-3} (lower). Bright (yellow) and dark (blue) colors indicate friction and thermal force dominant region, respectively.

Fig.5 (LHD) Distribution of parallel energy flux between different L_C flux tubes, for n_{LCFS}=2.0x10^{19} m^{-3} (a-c) and n_{LCFS}=5.0x10^{19} m^{-3} (d-f), at different radial positions; (a), (d) r_{eff}=0.60 m, (b), (e) 0.65 m and (c), (f) 0.72 m. Fluxes are averaged over each L_C group of $L_C < 10$m, $10 \le L_C < 10^2$ m, $10^2 \le L_C < 10^3$ m, $10^3 \le L_C < 10^4$ m and 10^4 m $\le L_C$. Energy flux is plotted for electron/ion conduction ($q_{//D}^{e,i}$) and electron convection ($q_{//V}^{e,i}$).

Fig.6 (LHD) (a) (c) Radial profiles of parallel impurity velocity, together with contribution of each term of eq.(3). The positive values represent radially outward flow. The velocities are shown for impurity $V_{//Z}^{imp}$ (thick solid line), electron thermal force $V_{//}^{the}$ (solid line), ion thermal force $V_{//}^{thi}$ (dashed line), friction force $V_{//}^{fric}$ (chain line), parallel electric field $V_{//}^{E}$ (dotted line). The velocity is averaged over poloidal and toroidal directions, and $V_{//}^{E}$ is estimated for Z=3. (b) (d) Impurity density summed over all charge states (solid line) and impurity ionization source (dotted line). The impurity density is normalized at r_{eff}=0.72 m (downstream). (a) (b) for n_{LCFS}=2.0x10^{19} m^{-3} and (c) (d) n_{LCFS}=5.0x10^{19} m^{-3}.

Fig.7 (LHD) (a) Two dimensional distribution of carbon density summed over all charge states and (b) force balance of $|V_{//}^{fric}|-|V_{//}^{thi}|$ in LHD, for n_{LCFS}=2.0 x10^{19} m^{-3} (upper) and 5.0 x10^{19} m^{-3} (lower). Bright (yellow) and dark (blue) colors indicate friction and thermal force dominant regions, respectively.

Fig.8 (a) Ratio of $n_{LCFS}^{imp} / n_{dowm}^{imp}$ as a function of collisionality. n_{LCFS}^{imp} and n_{dowm}^{imp} are the impurity density at LCFS and near divertor plates, respectively, summed up over all charge states (circles: impurity released at the divertor plate, triangles: impurity released at the first wall, black for LHD and grey for HL-2A) and $q_{//V}^{i} / q_{//D}^{i}$(=friction force / thermal force) at the upstream and downstream regions as a function of ν_{SOL}^{*ion} for (b) HL-2A and (c) LHD. In HL-2A, n_{dowm}^{imp} is obtained by averaging over all flux tubes in the outer and inner divertor legs. ν_{SOL}^{*ion} is evaluated around LCFS. In LHD, the variation of ν_{SOL}^{*ion} in the stochastic layers is indicated with the horizontal error bars. The high and low end values correspond to those at around LCFS and the edge surface layers, respectively. In (b) and (c), the downstream is defined as s=0~0.5 m (Fig.2(b)) for HL-2A, and r_{eff}=0.72 m for LHD (Fig.1(c)), i.e., near divertor plates, while the upstream is s=3~8 m (around X-point) for HL-2A and r_{eff}=0.65 m (in the stochastic region) for LHD.

Fig.9 Ionization source distribution of divertor recycling neutrals for (a) LHD (hydrogen) and (b) HL-2A (deuterium).

Fig.10 (LHD) Viewing area of VUV and EUV spectrometers of LHD.

Fig.11 Temperature dependence of carbon emission coefficients used for the present analysis; CIII 977 Å (dotted line), CIV 1548 Å (solid line), CV 40.27 Å for LHD (dashed-dotted line) and CV 2271 Å for HL-2A (dashed line). In the density range of 10^{18} to 10^{20} m^{-3}, there is almost no density dependence for these emissions.

Fig.12 (LHD) Radial profiles of (a) T_e and (b) n_e at outboard midplane, measured by Thomson scattering system (dots) (#81914) and simulated by 3D transport code EMC3-EIRENE (open circles) with n_{LCFS}~6.0×10^{19} m^{-3} and P_{SOL}=8MW and (c) emission coefficients of CIII, CIV and CV estimated from T_e profiles of Thomson data. CV emission coefficient obtained from 3D modeling ($D_{\perp}$=0.50 m^2/s and $\chi_{\perp}$=1.50

m^2/s) is also shown. In the modeling, perpendicular transport coefficients are set to $D_\perp$ =0.50 m^2/s and $\chi_\perp$=1.50 m^2/s for particle and energy transports, respectively, while the results with $\chi_\perp$ = 0.75, 0.38 and 0.19 m^2/s are also shown in (a). These coefficients are spatially constant. In the analysis in sections 3 and 4, $D_\perp$=0.50 m^2/s and $\chi_\perp$=1.50 m^2/s are used. Corresponding coordinate of r_{eff} is shown at the bottom. For the definition of r_{eff}, see the caption of Fig.1.

Fig.13 (HL-2A) Radial profiles of (a) T_e and (b) n_e at outboard midplane, measured by scanning probe (dots) (#12266) and simulated by 3D transport code EMC3-EIRENE (open circles) with n_{LCFS}~0.25x10^{19} m^{-3} and P_{SOL}=200kW. In the modeling, perpendicular transport coefficients are set to $D_\perp$=0.50 m^2/s and $\chi_\perp$=1.50 m^2/s for particle and energy transports, respectively. These coefficients are spatially constant.

Fig.14 (LHD) C^{3+} density distribution simulated by 3D transport code EMC3-EIRENE, for (a) n_{LCFS}=1.5x10^{19} and (b) 5.0x10^{19} m^{-3}. Viewing area of spectrometer is indicated with two horizontal dashed-dotted lines. Divertor impurity source with released energy of 0.05 eV and fixed sputtering coefficient of 0.01 are assumed in the simulation.

Fig. 15 (LHD) Line integrated CIV profiles measured with viewing area shown in Fig. 14 (b) for n_{LCFS}=1.1x10^{19} (dotted line) and 4.5x10^{19} m^{-3} (solid line). The vertical coordinate Z starts from the midplane and increases upward as shown in Fig.14 (b).

Fig. 16 (LHD) Line integrated CIV profiles in viewing area shown in Fig. 14 (b) simulated by 3D transport code EMC3-EIRENE for n_{LCFS}=1.5x10^{19} (dotted line) and 5.0x10^{19} m^{-3} (solid line). The impurity source is changed as (a) the divertor source with 0.05 eV and C_{sput}=0.01, (b) first wall with 0.05 eV and C_{sput}=0.01, (c) divertor source with 2eV and varied C_{sput}, (d) first wall with 2eV and varied C_{sput} and (e) all the sources combined ((a) and (b): chemical sputtering, (c) and (d): physical sputtering). The divertor source is distributed according to the plasma particle deposition pattern. The first wall source is assumed to be uniform.

Fig. 17 (LHD) Carbon emission normalized by electron density as a function of line averaged density $\bar{n}_e$, measured with viewing area of Fig. 10 (a). Open squares, solid

circles and solid diamonds denote CIII/n_e, CIV/n_e and CV/n_e, respectively.

Fig. 18 (LHD) Carbon emission normalized by electron density as a function of n_{LCFS}, simulated by 3D transport code EMC3-EIRENE with the viewing area of Fig.10 (a). Open squares, solid circles and solid diamonds denote CIII/n_e, CIV/n_e and CV/n_e. Parameters for impurity source assumed in simulation are the same as Fig.16. n_{LCFS} and $\overline{n}_e$ in Fig.17 are related as 0.8~1.0 $\overline{n}_e \sim n_{LCFS}$.

Fig. 19 (LHD) Radial profiles of carbon density simulated by 3D modeling with all sources combined corresponding to Fig.18 (e) at (a) n_{LCFS}=1.5x10^{19} m^{-3} and (b) n_{LCFS}=6.0x10^{19} m^{-3}. n_{imp} is density summed over all charge states.

Fig. 20 (HL-2A) C^{3+} density distribution simulated by 3D transport code EMC3-EIRENE for (a) n_{LCFS}=0.3x10^{19} and (b) 0.6x10^{19} m^{-3}. Viewing area of VUV spectrometer is indicated with two solid lines. The impurity is simulated with released energy of 0.05 eV and fixed sputtering coefficient of 0.01 at divertor plates.

Fig. 21 (HL-2A) Line integrated CIV profiles measured with viewing area shown in Fig. 20 (a) for $\overline{n}_e$=0.4x10^{19} m^{-3} (dashed line), 0.5~0.8x10^{19} m^{-3} (dotted line) and 2.5~2.6x10^{19} m^{-3} (solid line). $\overline{n}_e$ is related to n_{LCFS} in the modeling such as $n_{LCFS} = 0.2 \sim 0.3\overline{n}_e$. The vertical coordinate Z starts from the upper boundary of the viewing area and increases downward as shown in Fig.20 (a).

Fig. 22 (HL-2A) Line integrated CIV profiles simulated by 3D transport code EMC3-EIRENE in viewing area shown in Fig. 20 (a) for (a) divertor source with 0.05 eV, C_{sput}=0.01, (b) first wall with 0.05 eV, C_{sput}=0.01, (c) divertor source with 2eV and varied C_{sput}, (d) first wall with 2eV and varied C_{sput} and (e) all the sources combined. Dashed, dotted and solid lines denote n_{LCFS}=0.3, 0.4 and 0.6x10^{19} m^{-3}, respectively. The divertor source is distributed proportional to the plasma particle deposition pattern. The first wall source is assumed to be uniform.

Fig. 23 (HL-2A) Line integrated CIV profiles simulated by 3D transport code EMC3-EIRENE in viewing area shown in Fig. 20 (a); (a) divertor source with 0.05eV released energy and C_{sput} changed from 0.01 to 0.10 with increasing density and (b) baffle source with 0.05eV released energy and fixed C_{sput} of 0.01.

Fig. 24 (HL-2A) Carbon emission normalized by electron density as a function of the line averaged density, measured with viewing area of Fig. 20 (a) for CIII/n_e (open squares), CIV/n_e (solid circles) and CV/n_e (solid diamonds).

Fig. 25 (HL-2A) Carbon emission normalized by electron density as a function of n_{LCFS}, simulated by 3D transport code EMC3-EIRENE. Open squares, solid circles and solid diamonds denote CIII/n_e, CIV/n_e and CV/n_e, respectively. CV is multiplied by a factor of 10 in the ordinate. Parameters for impurity source assumed in simulation are the same as Fig.22.

Fig. 26 (HL-2A) Carbon emission normalized by electron density as a function of n_{LCFS}, simulated by 3D transport code EMC3-EIRENE; (a) divertor source with 0.05eV released energy and C_{sput} varied from 0.01 to 0.10 with density and (b) baffle source with 0.05eV released energy with fixed C_{sput} of 0.01. Open squares, solid circles and solid diamonds denote CIII/n_e, CIV/n_e and CV/n_e. CV is multiplied by a factor of 10 in the ordinate.

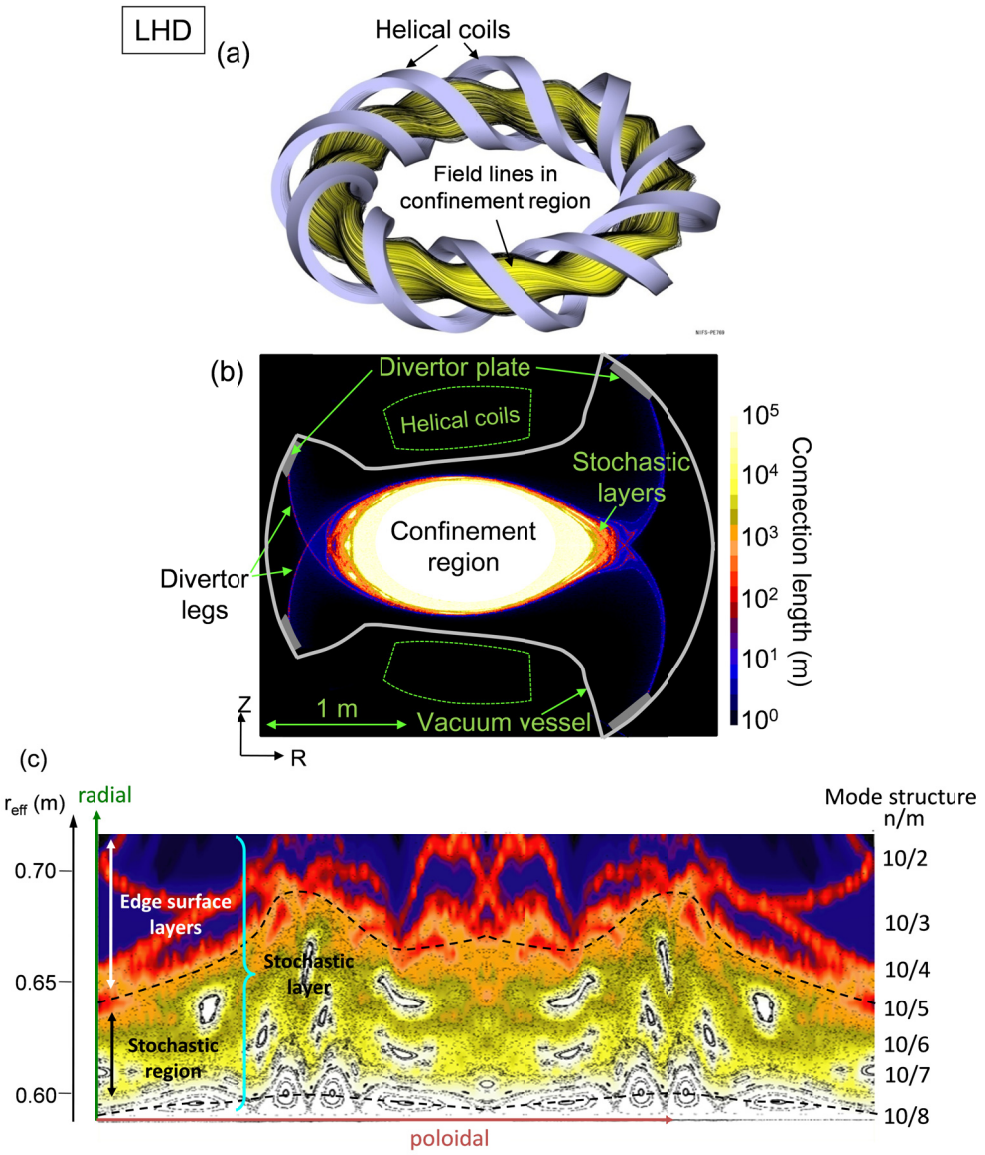

Fig.1 M. Kobayashi et al.

Fig.1 (LHD) (a) Magnetic field structure in confinement region of LHD and configuration of helical coils. Major and averaged minor radii are 3.75 and 0.70 m, respectively. (b) Poloidal cross section of LHD with divertor plates and divertor legs. Color represents the connection length (L_C). Divertor legs come out from confinement region in-between helical coils. (c) L_C distribution in poloidal and minor radial (r_{eff}) coordinate system. r_{eff} is defined by cylindrical approximation of volume enclosed by each radial surface of computational mesh. Dashed lines in (c) indicate boundaries of edge surface layers and stochastic region. In the present analysis, the term of stochastic layer is used to represent the entire edge region including both the edge surface layers and the stochastic region.

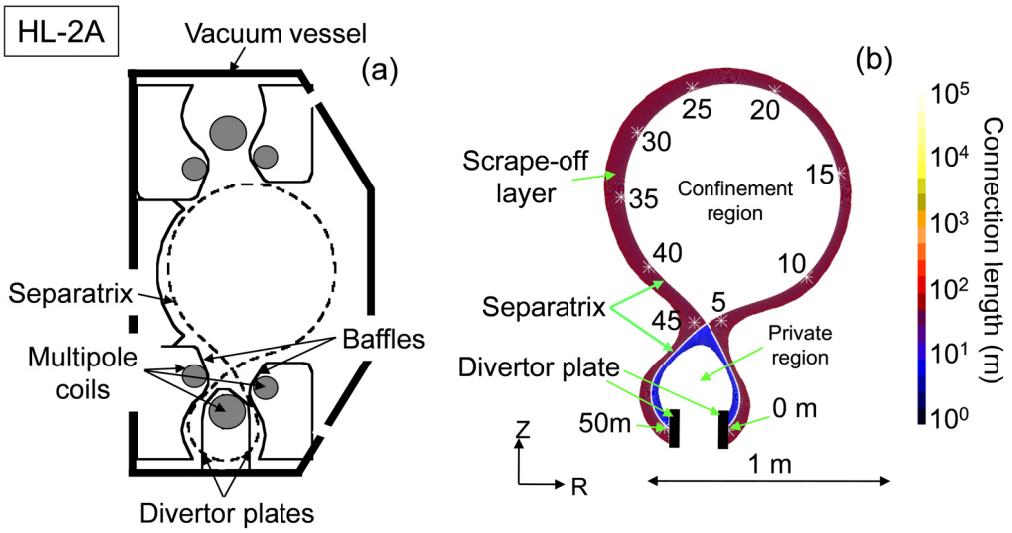

Fig.2 M. Kobayashi et al.

Fig.2 (HL-2A) (a) Schematic of HL-2A tokamak in poloidal cross section with vacuum vessel and divertor chamber/baffle. Three multi-pole coils create divertor configuration. Major and minor radii are 1.65 and 0.40 m, respectively. (b) L_C distribution in poloidal cross section. The numerals of 0 to 50 in (b) denote parallel distance, s, in meter along flux tubes with $L_C = 50 \pm 0.5\,m$, mapped to poloidal cross section.

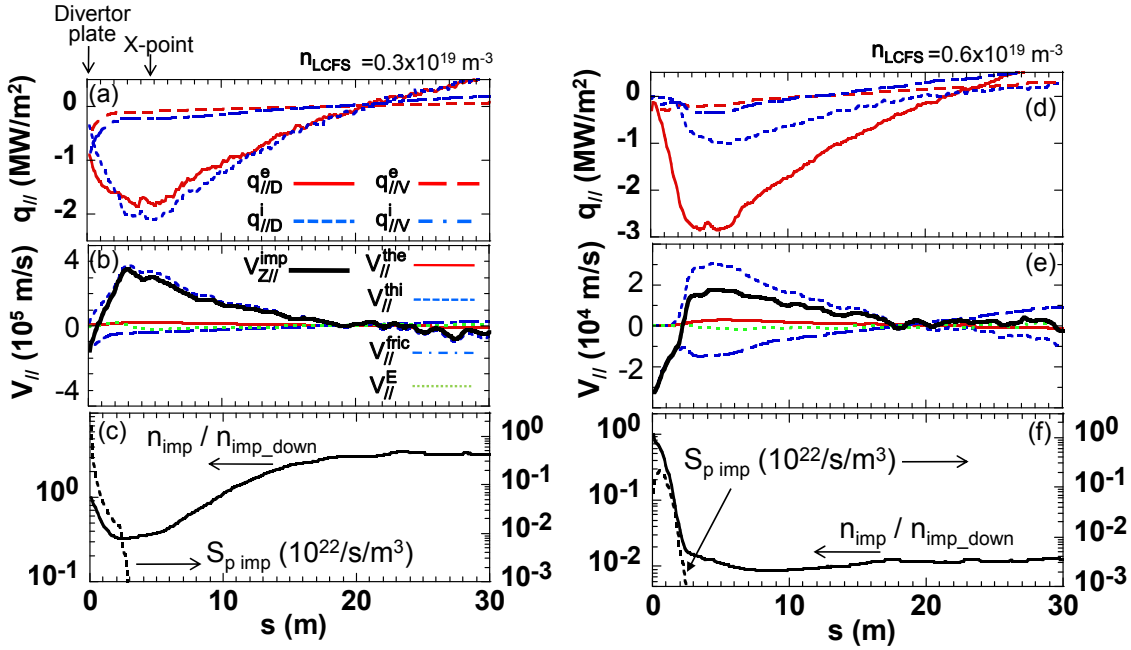

Fig.3 M. Kobayashi et al.

Fig.3 (HL-2A) Parallel profiles of various parameters along the field line of $L_C = 50 \pm 0.5\,m$ for densities of n_{LCFS}=0.3 x10^{19} m^{-3} (a-c) and 0.6 x10^{19} m^{-3} (d-f), respectively. Coordinate s is defined in Fig.2. (b). (a) and (d) show parallel energy flux of electron conduction, $q^e_{//D}$ (solid line), electron convection, $q^e_{//V}$ (dashed line), ion conduction, $q^i_{//D}$ (dotted line) and ion convection, $q^i_{//V}$ (chain line). (b) and (e) show parallel impurity velocity, $V^{imp}_{Z//}$ and contribution of each term on the right hand side of eq.(3), electron thermal force, $V_{//}{}^{the}$ (solid lines), ion thermal force, $V_{//}{}^{thi}$ (dashed lines), friction force, $V_{//}{}^{fric}$ (dashed-dotted lines) and // electric force, $V_{//}{}^{E}$ (dotted lines). For the definition, see the text. Note that the scale of vertical axes of (b) and (e) are different each other by one order of magnitude. (c) and (f) show carbon density summed over all charge states (solid lines) and carbon ionization source (dotted lines). The carbon density (n_{imp}) is normalized at the divertor plate (n_{imp_down}). Negative values of energy flux and velocity indicate direction towards outer divertor plates. X-point is located around s=5 m.

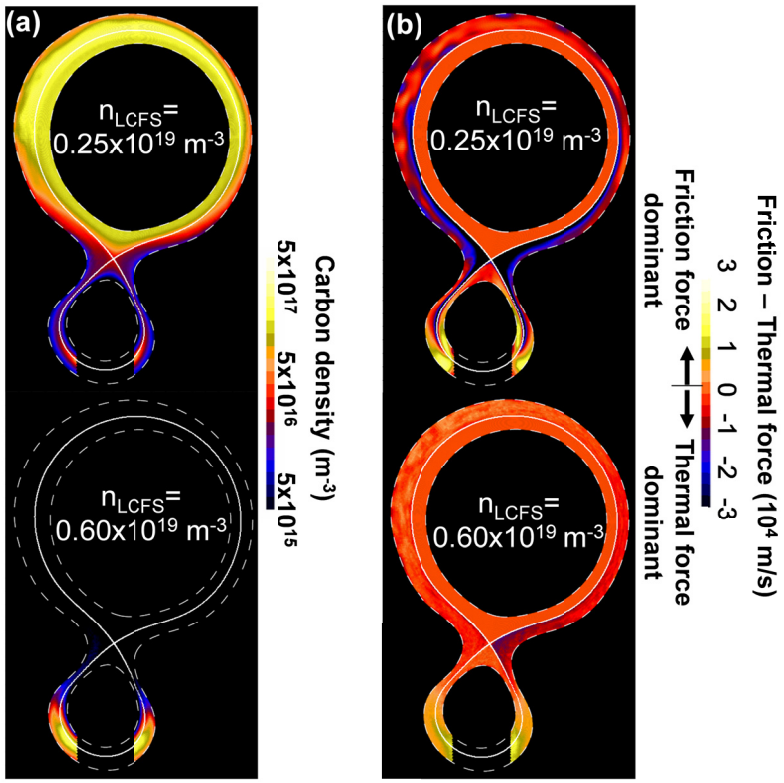

Fig.4 M. Kobayashi et al.

Fig.4 (HL-2A) (a) Two dimensional distribution of carbon density summed over all charge states and (b) force balance of $|V_{//}^{fric}|-|V_{//}^{thi}|$ in HL-2A, for n_{LCFS}=0.25 x10^{19} m^{-3} (upper) and 0.60 x10^{19} m^{-3} (lower). Bright (yellow) and dark (blue) colors indicate friction and thermal force dominant region, respectively.

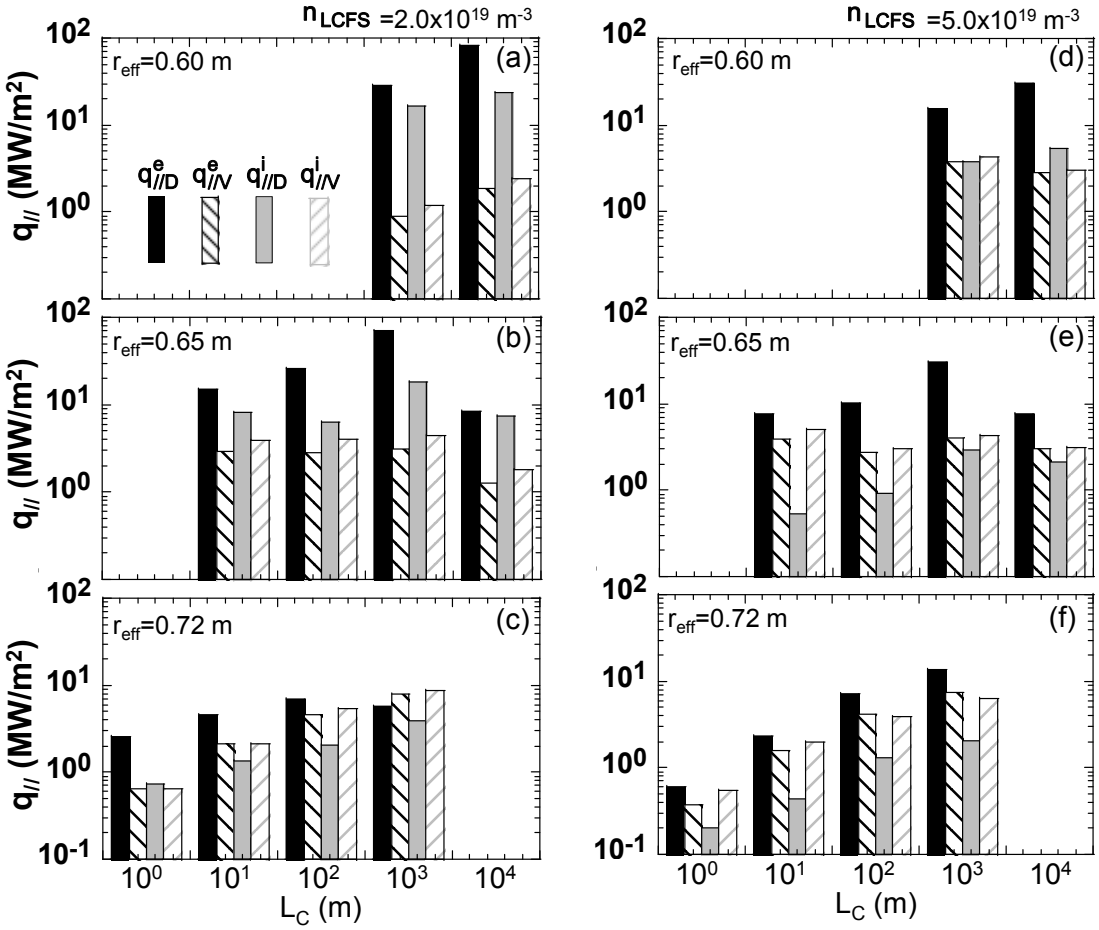

Fig.5 M. Kobayashi et al.

Fig.5 (LHD) Distribution of parallel energy flux between different L_C flux tubes, for n_{LCFS}=2.0x10^{19} m^{-3} (a-c) and n_{LCFS}=5.0x10^{19} m^{-3} (d-f), at different radial positions; (a), (d) r_{eff}=0.60 m, (b), (e) 0.65 m and (c), (f) 0.72 m. Fluxes are averaged over each L_C group of $L_C < 10$m, $10 \le L_C < 10^2$ m, $10^2 \le L_C < 10^3$ m, $10^3 \le L_C < 10^4$ m and 10^4 m $\le L_C$. Energy flux is plotted for electron/ion conduction ($q_{//D}^{e,i}$) and electron convection ($q_{//V}^{e,i}$).

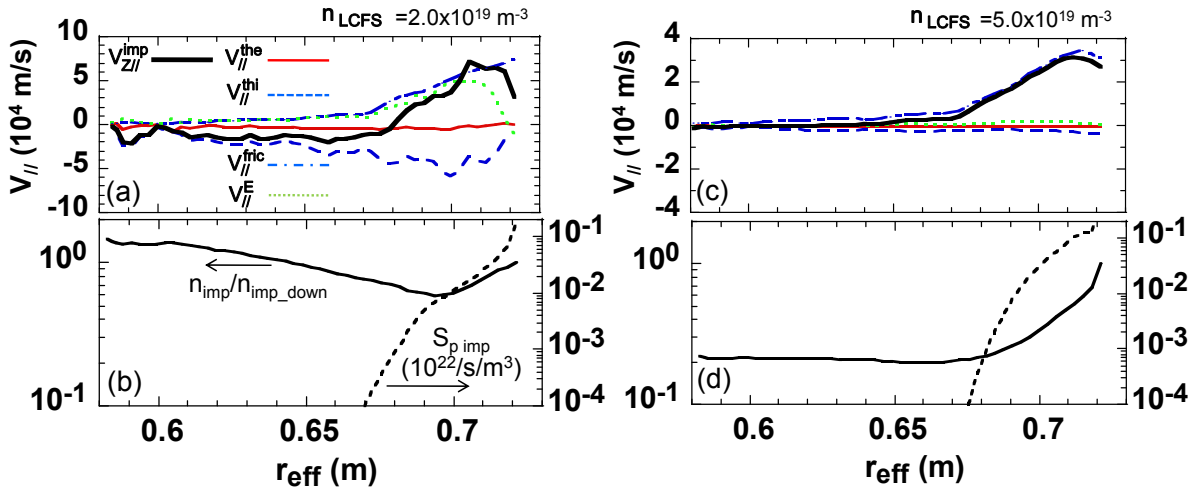

Fig.6 M. Kobayashi et al.

Fig.6 (LHD) (a) (c) Radial profiles of parallel impurity velocity, together with contribution of each term of eq.(3). The positive values represent radially outward flow. The velocities are shown for impurity $V_{//Z}^{imp}$ (thick solid line), electron thermal force $V_{//}^{the}$ (solid line), ion thermal force $V_{//}^{thi}$ (dashed line), friction force $V_{//}^{fric}$ (chain line), parallel electric field $V_{//}^{E}$ (dotted line). The velocity is averaged over poloidal and toroidal directions, and $V_{//}^{E}$ is estimated for Z=3. (b) (d) Impurity density summed over all charge states (solid line) and impurity ionization source (dotted line). The impurity density is normalized at r_{eff}=0.72 m (downstream). (a) (b) for n_{LCFS}=2.0x10^{19} m^{-3} and (c) (d) n_{LCFS}=5.0x10^{19} m^{-3}.

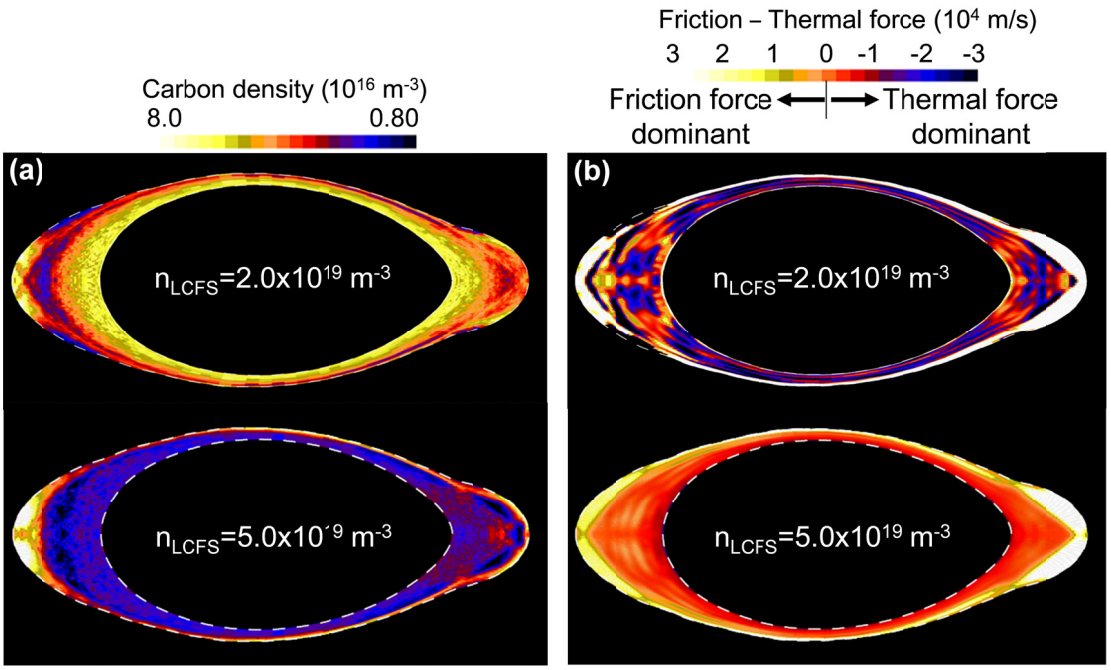

Fig.7 M. Kobayashi et al.

Fig.7 (LHD) (a) Two dimensional distribution of carbon density summed over all charge states and (b) force balance of $|V_{//}^{fric}|-|V_{//}^{thi}|$ in LHD, for n_{LCFS}=2.0 x10^{19} m^{-3} (upper) and 5.0 x10^{19} m^{-3} (lower). Bright (yellow) and dark (blue) colors indicate friction and thermal force dominant regions, respectively.

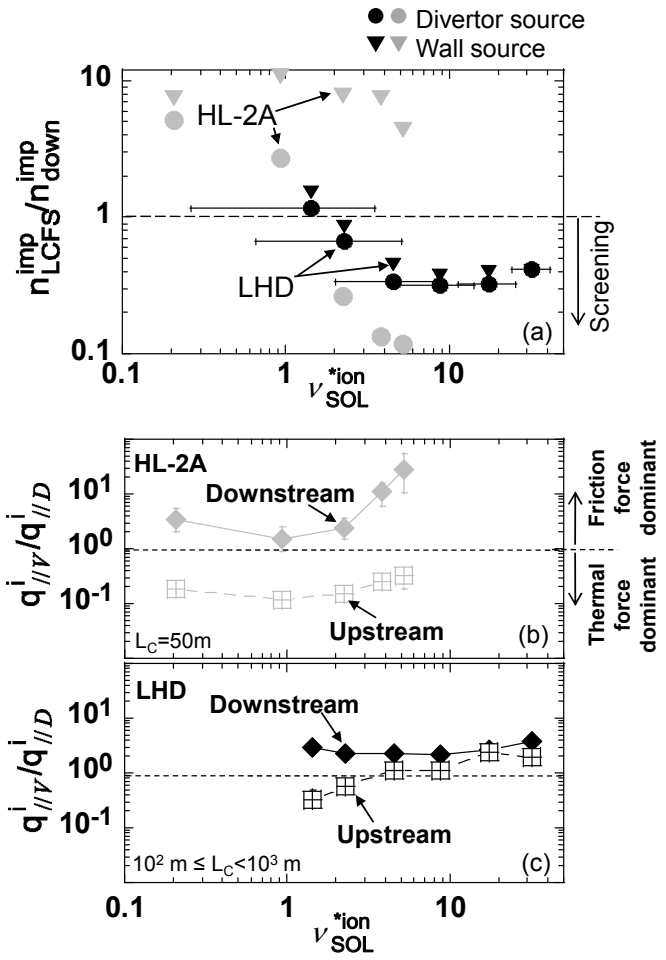

Fig.8 M. Kobayashi et al.

Fig.8 (a) Ratio of $n^{imp}_{LCFS}/n^{imp}_{dowm}$ as a function of collisionality. n^{imp}_{LCFS} and n^{imp}_{dowm} are the impurity density at LCFS and near divertor plates, respectively, summed up over all charge states (circles: impurity released at the divertor plate, triangles: impurity released at the first wall, black for LHD and grey for HL-2A) and $q^i_{//V}/q^i_{//D}$(=friction force / thermal force) at the upstream and downstream regions as a function of ν^{*ion}_{SOL} for (b) HL-2A and (c) LHD. In HL-2A, n^{imp}_{dowm} is obtained by averaging over all flux tubes in the outer and inner divertor legs. ν^{*ion}_{SOL} is evaluated around LCFS. In LHD, the variation of ν^{*ion}_{SOL} in the stochastic layers is indicated with the horizontal error bars.

The high and low end values correspond to those at around LCFS and the edge surface layers, respectively. In (b) and (c), the downstream is defined as s=0~0.5 m (Fig.2(b)) for HL-2A, and r_{eff}=0.72 m for LHD (Fig.1(c)), i.e., near divertor plates, while the upstream is s=3~8 m (around X-point) for HL-2A and r_{eff}=0.65 m (in the stochastic region) for LHD.

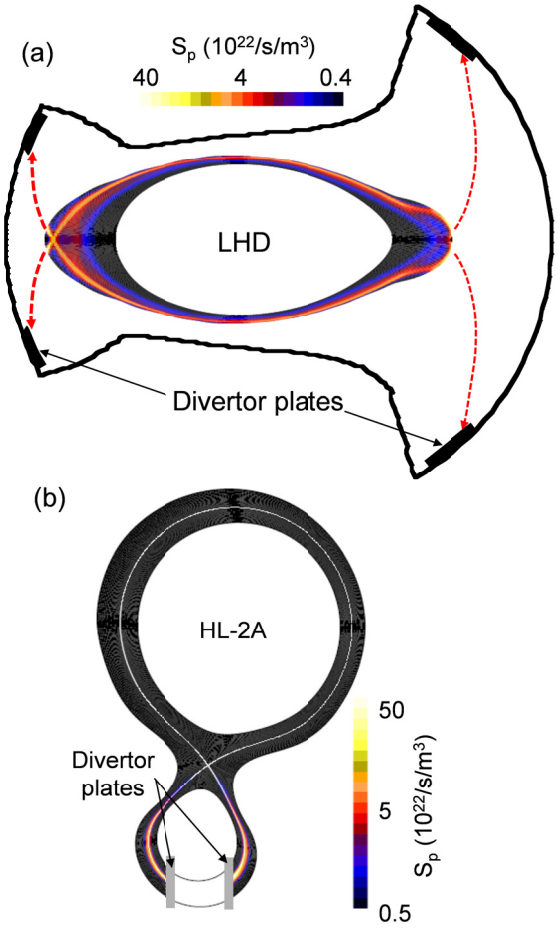

Fig.9 M. Kobayashi et al.

Fig.9 Ionization source distribution of divertor recycling neutrals for (a) LHD (hydrogen) and (b) HL-2A (deuterium).

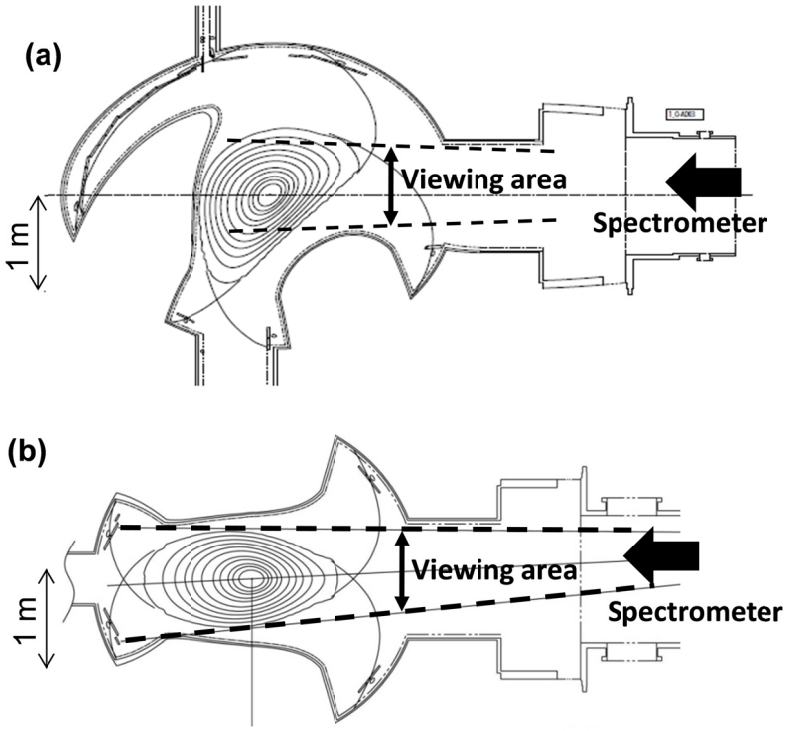

Fig.10 M. Kobayashi et al.

Fig.10 (LHD) Viewing area of VUV and EUV spectrometers of LHD.

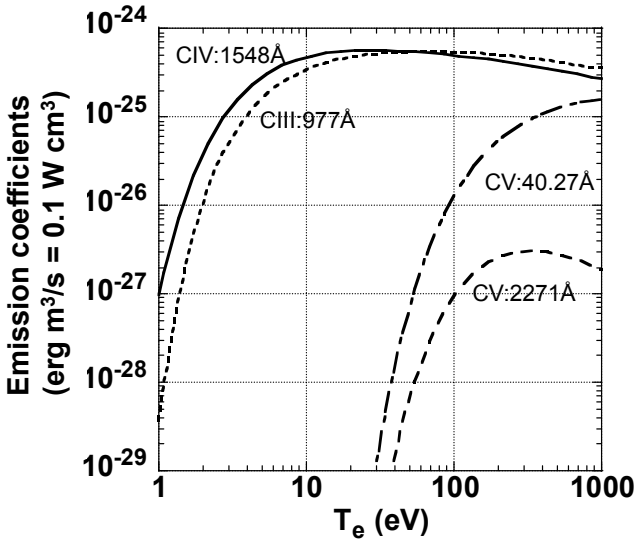

Fig.11 M. Kobayashi et al.

Fig.11 Temperature dependence of carbon emission coefficients used for the present analysis; CIII 977 Å (dotted line), CIV 1548 Å (solid line), CV 40.27 Å for LHD (dashed-dotted line) and CV 2271 Å for HL-2A (dashed line). In the density range of 10^{18} to 10^{20} m^{-3}, there is almost no density dependence for these emissions.

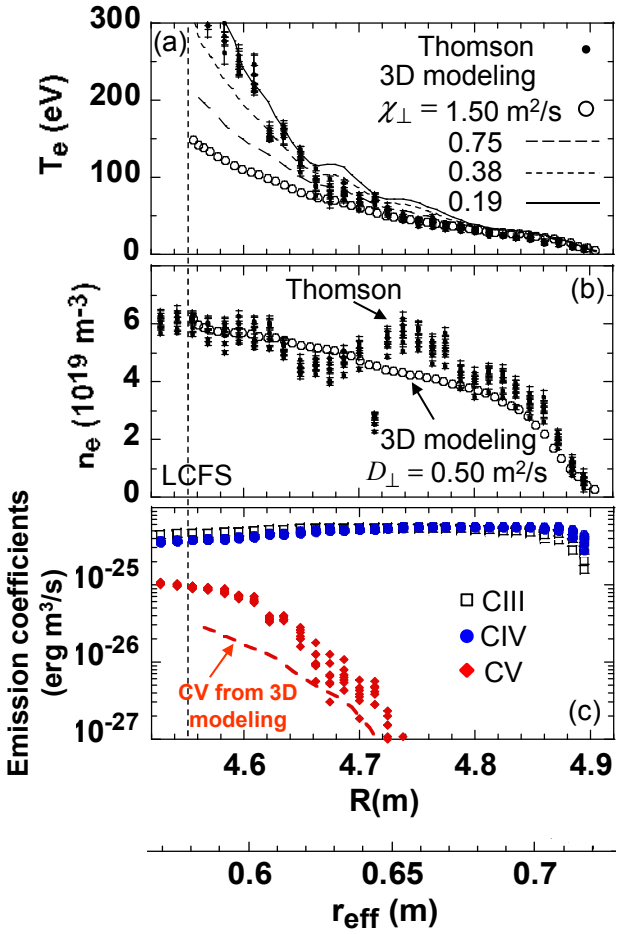

Fig.12 M. Kobayashi et al.

Fig.12 (LHD) Radial profiles of (a) T_e and (b) n_e at outboard midplane, measured by Thomson scattering system (dots) (#81914) and simulated by 3D transport code EMC3-EIRENE (open circles) with n_{LCFS}~6.0x10^{19} m^{-3} and P_{SOL}=8MW and (c) emission coefficients of CIII, CIV and CV estimated from T_e profiles of Thomson data. CV emission coefficient obtained from 3D modeling ($D_\perp$=0.50 m^2/s and $\chi_\perp$=1.50 m^2/s) is also shown. In the modeling, perpendicular transport coefficients are set to $D_\perp$ =0.50 m^2/s and $\chi_\perp$=1.50 m^2/s for particle and energy transports, respectively, while the results with $\chi_\perp$ = 0.75, 0.38 and 0.19 m^2/s are also shown in (a). These coefficients are spatially constant. In the analysis in sections 3 and 4, $D_\perp$=0.50 m^2/s and $\chi_\perp$=1.50 m^2/s are used. Corresponding coordinate of r_{eff} is shown at the bottom. For the definition of r_{eff}, see the caption of Fig.1.

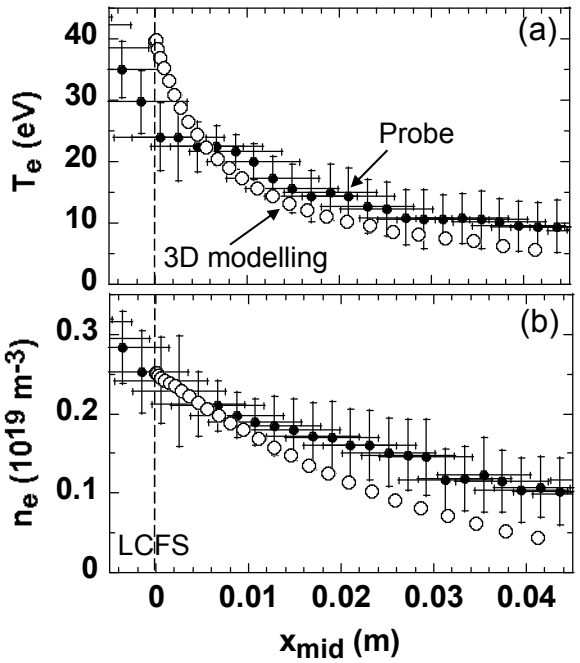

Fig.13 M. Kobayashi et al.

Fig.13 (HL-2A) Radial profiles of (a) T_e and (b) n_e at outboard midplane, measured by scanning probe (dots) (#12266) and simulated by 3D transport code EMC3-EIRENE (open circles) with n_{LCFS}~0.25×10^{19} m^{-3} and P_{SOL}=200kW. In the modeling, perpendicular transport coefficients are set to $D_\perp$=0.50 m^2/s and $\chi_\perp$=1.50 m^2/s for particle and energy transports, respectively. These coefficients are spatially constant.

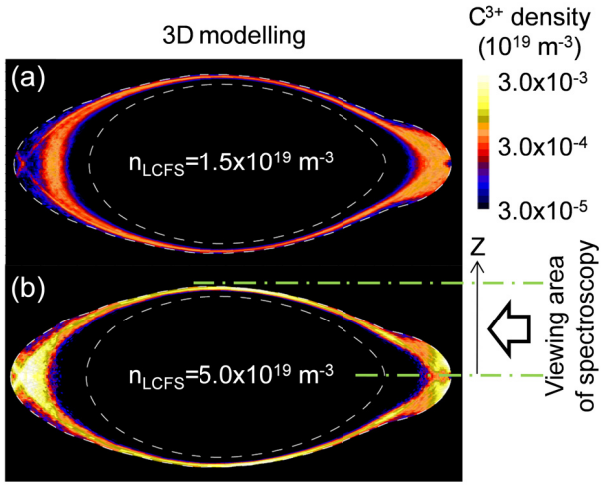

Fig. 14 M. Kobayashi et al.

Fig.14 (LHD) C^{3+} density distribution simulated by 3D transport code EMC3-EIRENE, for (a) $n_{LCFS}=1.5x10^{19}$ and (b) $5.0x10^{19}$ m^{-3}. Viewing area of spectrometer is indicated with two horizontal dashed-dotted lines. Divertor impurity source with released energy of 0.05 eV and fixed sputtering coefficient of 0.01 are assumed in the simulation.

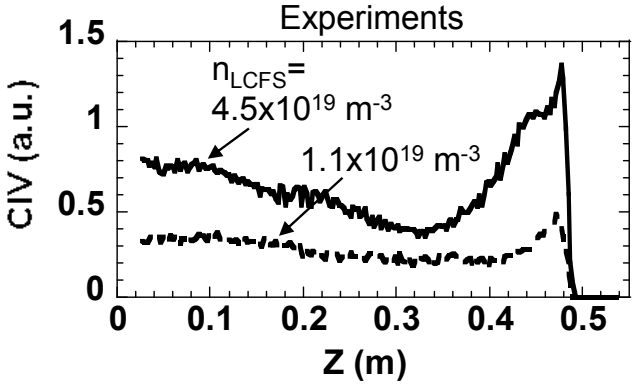

Fig. 15 M. Kobayashi et al.

Fig. 15 (LHD) Line integrated CIV profiles measured with viewing area shown in Fig. 14 (b) for n_{LCFS}=1.1x10^{19} (dotted line) and 4.5x10^{19} m^{-3} (solid line). The vertical coordinate Z starts from the midplane and increases upward as shown in Fig.14 (b).

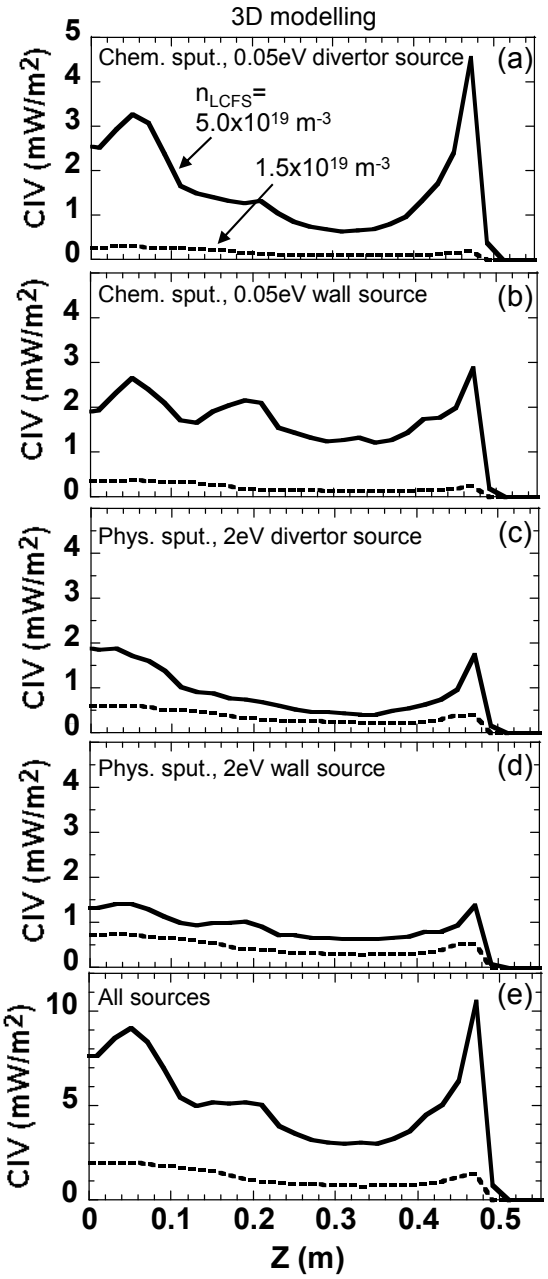

Fig. 16 M. Kobayashi et al.

Fig. 16 (LHD) Line integrated CIV profiles in viewing area shown in Fig. 14 (b) simulated by 3D transport code EMC3-EIRENE for n_{LCFS}=1.5x10^{19} (dotted line) and 5.0x10^{19} m^{-3} (solid line). The impurity source is changed as (a) the divertor source with 0.05 eV and C_{sput}=0.01, (b) first wall with 0.05 eV and C_{sput}=0.01, (c) divertor source with 2eV and varied C_{sput}, (d) first wall with 2eV and varied C_{sput} and (e) all the sources combined ((a) and (b): chemical sputtering, (c) and (d): physical sputtering). The divertor source is distributed according to the plasma particle deposition pattern. The first wall source is assumed to be uniform.

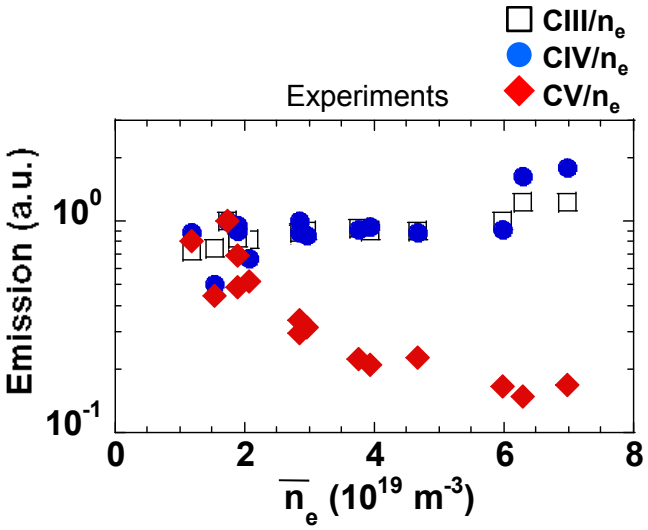

Fig. 17 M. Kobayashi et al.

Fig. 17 (LHD) Carbon emission normalized by electron density as a function of line averaged density $\overline{n}_e$, measured with viewing area of Fig. 10 (a). Open squares, solid circles and solid diamonds denote CIII/n_e, CIV/n_e and CV/n_e, respectively.

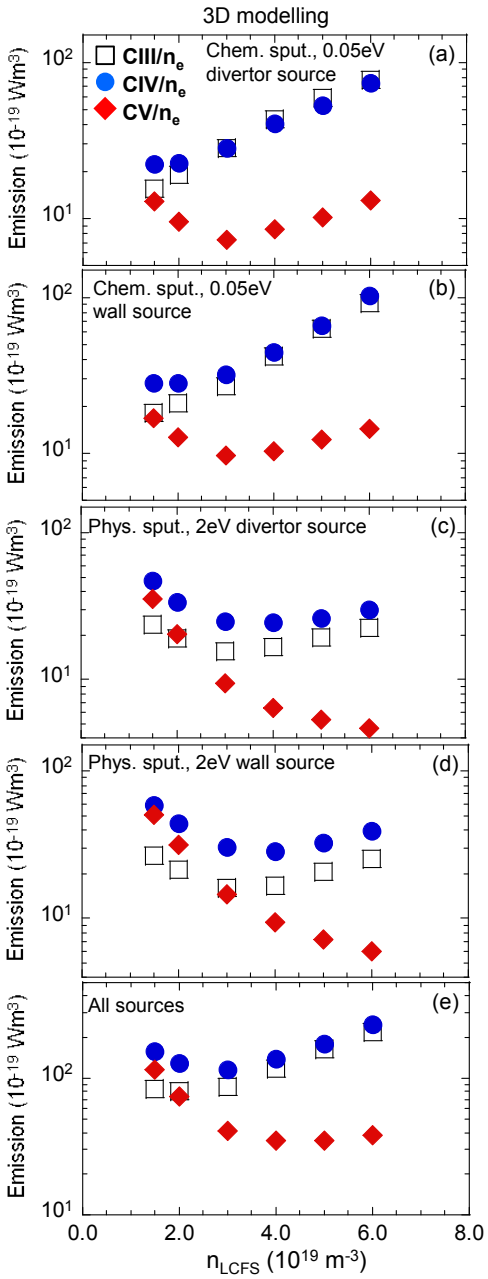

Fig. 18 M. Kobayashi et al.

Fig. 18 (LHD) Carbon emission normalized by electron density as a function of n_{LCFS}, simulated by 3D transport code EMC3-EIRENE with the viewing area of Fig.10 (a). Open squares, solid circles and solid diamonds denote CIII/n_e, CIV/n_e and CV/n_e. Parameters for impurity source assumed in simulation are the same as Fig.16. n_{LCFS} and $\overline{n}_e$ in Fig.17 are related as 0.8~1.0 $\overline{n}_e \sim n_{LCFS}$.

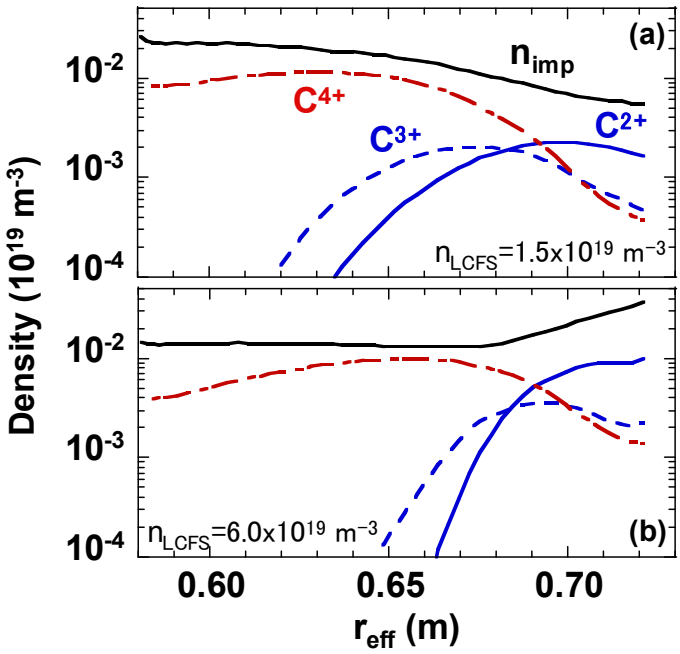

Fig.19 M. Kobayashi et al.

Fig. 19 (LHD) Radial profiles of carbon density simulated by 3D modeling with all sources combined corresponding to Fig.18 (e) at (a) n_{LCFS}=1.5x10^{19} m^{-3} and (b) n_{LCFS}=6.0x10^{19} m^{-3}. n_{imp} is density summed over all charge states.

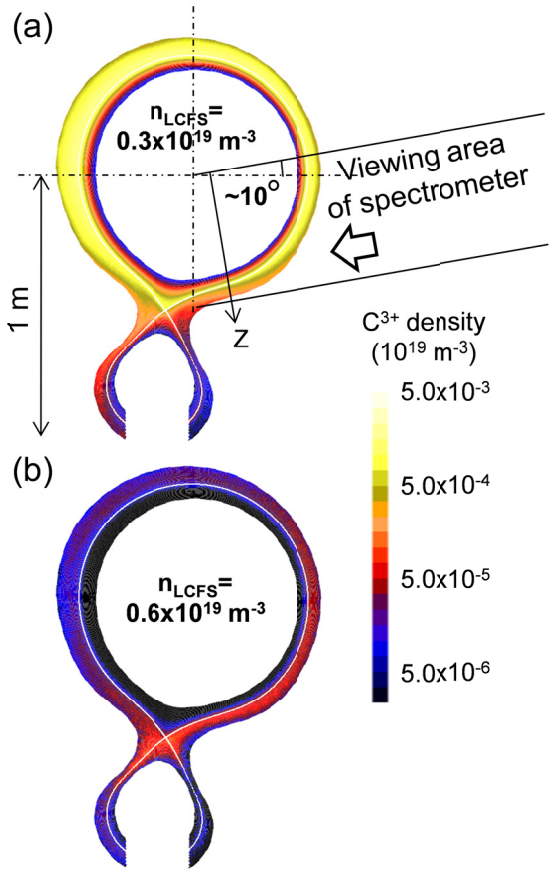

Fig. 20 M. Kobayashi et al.

Fig. 20 (HL-2A) C^{3+} density distribution simulated by 3D transport code EMC3-EIRENE for (a) n_{LCFS}=0.3x10^{19} and (b) 0.6x10^{19} m^{-3}. Viewing area of VUV spectrometer is indicated with two solid lines. The impurity is simulated with released energy of 0.05 eV and fixed sputtering coefficient of 0.01 at divertor plates.

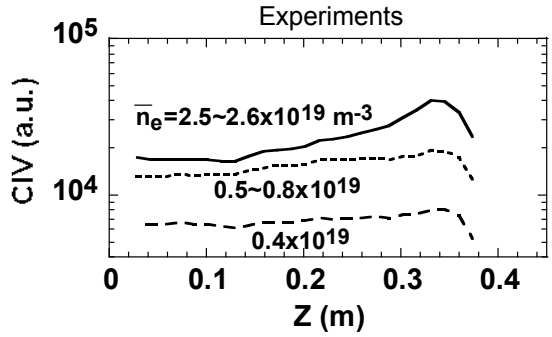

Fig. 21 M. Kobayashi et al.

Fig. 21 (HL-2A) Line integrated CIV profiles measured with viewing area shown in Fig. 20 (a) for $\overline{n}_e$=0.4x10^{19} m^{-3} (dashed line), 0.5~0.8x10^{19} m^{-3} (dotted line) and 2.5~2.6x10^{19} m^{-3} (solid line). $\overline{n}_e$ is related to n_{LCFS} in the modeling such as $n_{LCFS} = 0.2 \sim 0.3\overline{n}_e$. The vertical coordinate Z starts from the upper boundary of the viewing area and increases downward as shown in Fig.20 (a).

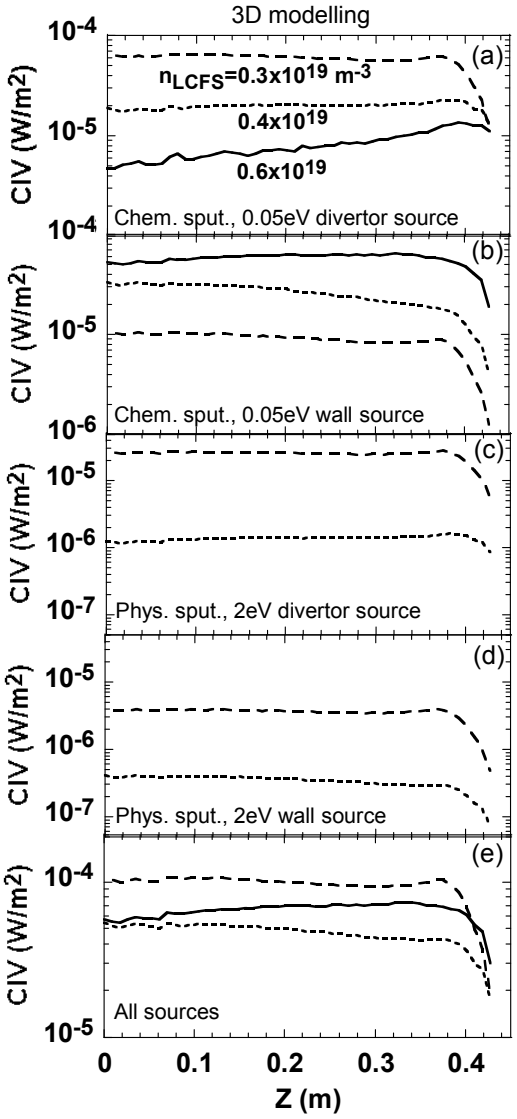

Fig. 22 M. Kobayashi et al.

Fig. 22 (HL-2A) Line integrated CIV profiles simulated by 3D transport code EMC3-EIRENE in viewing area shown in Fig. 20 (a) for (a) divertor source with 0.05 eV, C_{sput}=0.01, (b) first wall with 0.05 eV, C_{sput}=0.01, (c) divertor source with 2eV and varied C_{sput}, (d) first wall with 2eV and varied C_{sput} and (e) all the sources combined. Dashed, dotted and solid lines denote n_{LCFS}=0.3, 0.4 and 0.6x10^{19} m^{-3}, respectively. The divertor source is distributed proportional to the plasma particle deposition pattern. The first wall source is assumed to be uniform.

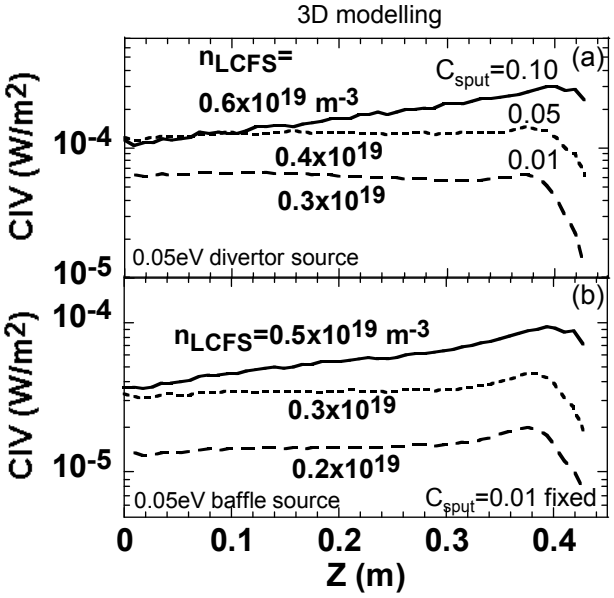

Fig. 23 M. Kobayashi et al.

Fig. 23 (HL-2A) Line integrated CIV profiles simulated by 3D transport code EMC3-EIRENE in viewing area shown in Fig. 20 (a); (a) divertor source with 0.05eV released energy and C_{sput} changed from 0.01 to 0.10 with increasing density and (b) baffle source with 0.05eV released energy and fixed C_{sput} of 0.01.

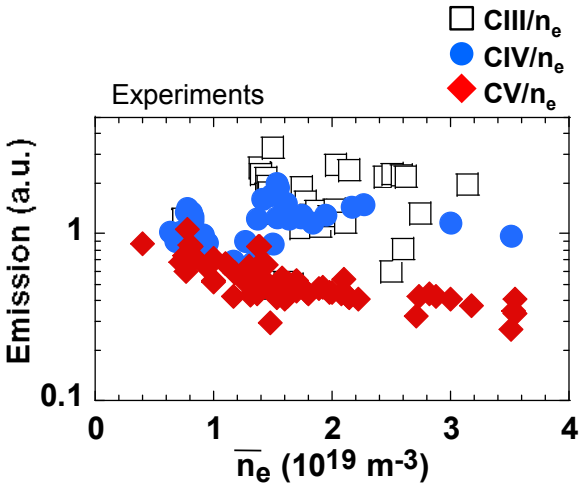

Fig. 24 M. Kobayashi et al.

Fig. 24 (HL-2A) Carbon emission normalized by electron density as a function of the line averaged density, measured with viewing area of Fig. 20 (a) for CIII/n_e (open squares), CIV/n_e (solid circles) and CV/n_e (solid diamonds).

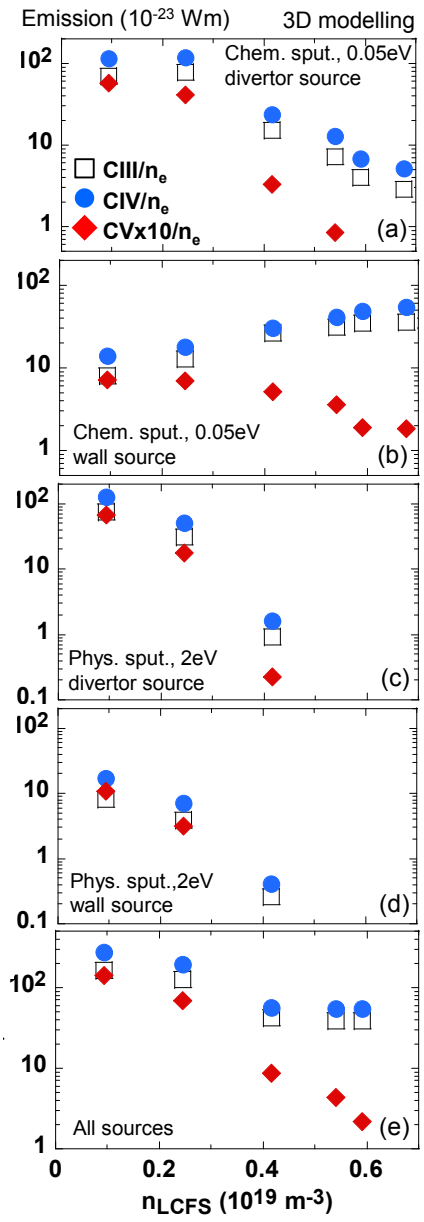

Fig. 25 M. Kobayashi et al.

Fig. 25 (HL-2A) Carbon emission normalized by electron density as a function of n_{LCFS}, simulated by 3D transport code EMC3-EIRENE. Open squares, solid circles and solid diamonds denote CIII/n_e, CIV/n_e and CV/n_e, respectively. CV is multiplied by a factor of 10 in the ordinate. Parameters for impurity source assumed in simulation are the same as Fig.22.

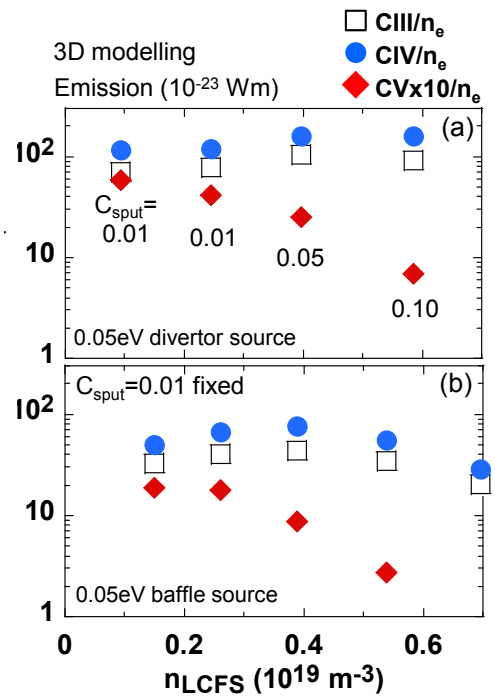

Fig. 26 M. Kobayashi et al.

Fig. 26 (HL-2A) Carbon emission normalized by electron density as a function of n_{LCFS}, simulated by 3D transport code EMC3-EIRENE; (a) divertor source with 0.05eV released energy and C_{sput} varied from 0.01 to 0.10 with density and (b) baffle source with 0.05eV released energy with fixed C_{sput} of 0.01. Open squares, solid circles and solid diamonds denote CIII/n_e, CIV/n_e and CV/n_e. CV is multiplied by a factor of 10 in the ordinate.